arXiv:1901.07124v3 [cs.CV] 10 Sep 2019

Linearized Multi-Sampling for Differentiable Image Transformation

Wei Jiang[1] Weiwei Sun[1] Andrea Tagliasacchi[1,2] Eduard Trulls[2] Kwang Moo Yi[1]

[1]Visual Computing Group, University of Victoria [2]Google Research

{jiangwei, weiweisun, kyi}@uvic.ca, {taglia, trulls}@google.com

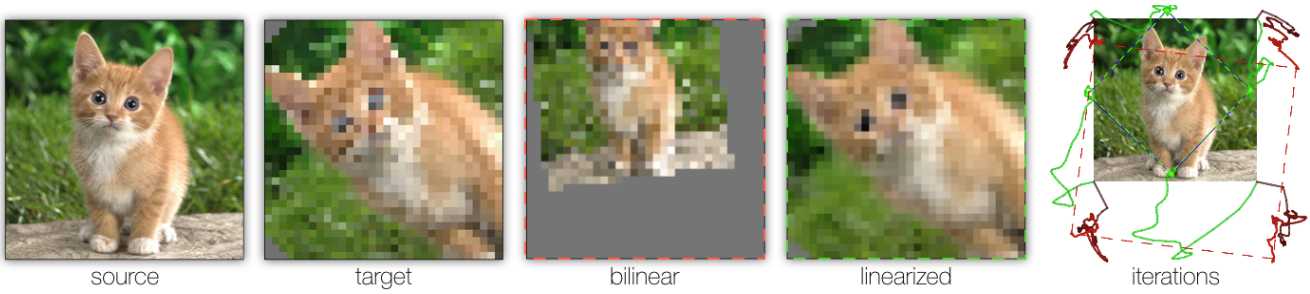


Figure 1: **Image alignment example -** We iteratively find the image transformation parameters that produce the downsampled *target* image when applied to the *source* image using different sampling strategies. We visualize the transformed source image at convergence when using ***bilinear*** sampling and the proposed ***linearized*** sampling. We further display the optimization path – *iterations* – for each method. The proposed linearized sampling provides improved gradients, leading to better convergence.

Abstract

We propose a novel image sampling method for differentiable image transformation in deep neural networks. The sampling schemes currently used in deep learning, such as Spatial Transformer Networks, rely on bilinear interpolation, which performs poorly under severe scale changes, and more importantly, results in poor gradient propagation. This is due to their strict reliance on direct neighbors. Instead, we propose to generate random auxiliary samples in the vicinity of each pixel in the sampled image, and create a linear approximation with their intensity values. We then use this approximation as a differentiable formula for the transformed image.

We demonstrate that our approach produces more representative gradients with a wider basin of convergence for image alignment, which leads to considerable performance improvements when training networks for classification tasks. This is not only true under large downsampling, but also when there are no scale changes. We compare our approach with multi-scale sampling and show that we outperform it. We then demonstrate that our improvements to the sampler are compatible with other tangential improvements to Spatial Transformer Networks and that it further improves their performance. [1]

[1] Code and models are available at https://github.com/vcg-uvic/linearized_multisampling_release.

1. Introduction

The seminal work of [17] introduced Spatial Transformer Networks (STN), a differentiable component that allows for spatial manipulation of image data by deep networks. It has since become commonplace to include attention mechanisms in deep architectures in the form of image transformation operations. STNs have been applied to object detection [10], segmentation [15, 24], dense image captioning [19], local correspondence for image classification [1], local features [38, 28, 27], and as a tool for local hard attention [21]. Regardless of application and architecture, all of these methods rely on bilinear interpolation.

A major drawback of bilinear interpolation is that it is *extremely* local – it considers only the four closest pixel neighbors of the query. As this sampling does not account for the magnitude of the applied transformation, the performance of networks that rely on it degrades when scale changes are severe, as for example shown in Fig. 1. This shortcoming of the differentiable sampler was already hinted at in the original STN paper [17], but never fully investigated. Note that this is a problem in practice, as applications that leverage attention mechanisms often transform the image to a resolution much lower than the original [37, 28, 15]. Furthermore, STNs are typically used as pre-alignment networks for classification [17, 23]. The inability of the bilinear sampler in the STN to cope with large downsampling results in increased capacity requirements for the classification net-

work – this extra capacity will be needed to learn invariance to transformations the STN was not able to capture. We show that this is indeed the case by demonstrating that a better classification accuracy can be achieved with the *same* network by replacing the sampling operation with ours.

Several methods have been proposed to improve the stability and robustness of networks that employ bilinear sampling. For example, Lin *et al*. [23] introduced inverse compositional spatial transformer networks (ICSTN), which decompose transformations into smaller ones. Jia *et al*. [18] proposed to warp features rather than images. Shu *et al*. [32] proposed a hierarchical strategy incorporating flow-fields. However, all of these methods still rely on heavily localized bilinear interpolation when it comes to computing the values of individual pixels.

Instead, we take our inspiration from the well-known Lucas-Kanade (LK) optical flow algorithm [26, 2], and linearize the interpolation process by building a suitable first-order approximation by randomly sampling the neighborhood of the query. These auxiliary samples are created in the *transformed* image domain, so that their spatial locations take into account the transformation applied to the image. In other words, the resulting gradients are *transformation-aware*, and able to capture how the image changes according to the transformation.

However, this process can cause sample locations to collapse, as the transformation may warp them all to a single pixel – for example, when the transformer zooms into to a small area of the image. To overcome this issue, we propose an effective solution that perturbs the auxiliary samples after warping. This two-stage strategy allows our approach to deal with *any* type of affine transformation.

Our experiments demonstrate that this allows for a wider basin of convergence for image alignment, which helps the underlying optimization task. Most importantly, any network with embedded attention mechanisms, *i.e*. anywhere differentiable image transformation is required, should perform better when substituting standard bilinear interpolation with our approach. We demonstrate this by adding our sampling method to ICSTN [23], and show that we are able to not only reduce its error rate by 14.6% (relative) even *without* down sampling, but also that we effectively eliminate the harming effect of 4x downsampling on the performance of the classifier (error at 1x is 4.85% and at 4x is 4.86%). This means that we can use a classification network that is 11 times smaller than the original, without any performance loss.

2. Related work

There is a vast amount of work in the literature on estimating spatial transformations, with key applications to image registration problems, going back to the pioneering work of Lucas and Kanade [26]. Here we review previous efforts on image alignment and sampling techniques, particularly with regards to their use in deep learning.

Linearization. The Lucas & Kanade (LK) algorithm [26] predicts the transformation parameters using linear regression. It mathematically linearizes the relationship between pixel intensities and pixel locations by taking the first-order Taylor approximation. In this manner, the sampling process can be enhanced by enforcing linear relationships during the individual pixel sampling. This approach has proved greatly successful in many applications such as optical flow estimation [3]. Linearization is also widely utilized to improve the consistency of the pixel values in image filtering [16].

Multisampling. Multisampling is a common approach to enhance the reliability of sampling strategies. For example, one can sample multiple nearby pixels before feeding them to a classifier, jointly smoothing the scores from a pixel and its neighbors [40, 9]. Non-local means [5] computation can be sped up by Markov Chain Monte Carlo (MCMC) sampling [8]. Sampling can also be employed to compute finite differences at large stencils to produce gradient estimates that are less sensitive to noise and discontinuities [34].

In the context of deep learning. Early efforts in deep learning for computer vision were limited by their inability to manipulate input data, a crucial requirement in achieving spatial invariance. Jaderberg *et al*. proposed to address this shortcoming with Spatial Transformer Networks [17], which introduced the concept of a differentiable transformation to actively manipulate the input image or the feature maps. This effectively enabled learning hard attention mechanisms in and end-to-end fashion. To achieve this, they introduced a differentiable sampling operation, making it possible to propagate the loss in subsequent tasks with respect to the parameters of the predicted transformation.

STNs are widely used in applications that operate on image patches [36, 32, 39, 4]. Modern methods, such as Wang *et al*. [35], improve the patch sampling through an in-network transformation. Qi *et al*. introduced PointNet [30], a deep network for 3D point cloud segmentation which relies on STN to learn to transform the data into a canonical form before giving it to the network. Nevertheless, the paper reports only marginal performance improvements with the use of the STN, which demonstrates there is potential for further research in this area.

Several methods use bilinear sampling without explicitly learning a transformation. LIFT [37] and LF-Net [28] relied on STN to warp image patches and learn local features in an end-to-end manner, with the transformation parameters given by specially-tailored networks (*e.g*. keypoint detection). AffNet [27] applied a similar strategy to learn affine-covariant regions. Polar Transformer Networks [12] were used by [11] to build scale-invariant descriptors by transforming the input patch into log-polar space.

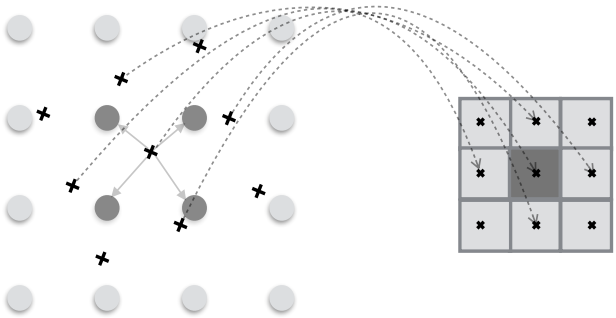


Figure 2: **Bilinear sampling –** To sample a 3×3 image on the right from the image on the left, each pixel is queried in order to find the exact corresponding point in the left image, according to a given transformation. As illustrated by the central pixel, the intensities are computed through the nearest neighbors by bilinear interpolation. Note that, even when the pixels on the right fall into further away regions, the interpolation will *always* be performed from their direct neighbors.

Bilinear sampling has also been used in the context of image upsampling, depth estimation, and segmentation [14, 7, 15, 25, 31]. For example, in Mask R-CNN [15], the region of interest alignment layer mainly relies on bilinear sampling/interpolation. These methods could also potentially benefit from enhanced sampling.

Current limitations of Spatial Transformers. Despite its popularity, in this paper we show how the bilinear sampler utilized in the STN framework is inherently unreliable and lacks robustness. Several variants have been recently proposed in order to cope with these shortcomings.

Jia *et al*. [18] showed how to exploit patterns found in the feature map deformations throughout the network layers that are insensitive to bilinear interpolation, thus boosting the accuracy of STN. Chang *et al*. [6] trained a deep network with a Lucas-Kanade layer to perform coarse-to-fine image alignment. The inverse compositional network proposed in [23] passes the transformation parameters instead of the transformed image in the forward pass in order to mitigate errors in the bilinear sampling. Recently, a hierarchical strategy was proposed to deal with transformations at multiple levels [32], by incorporating a U-Net [31], providing richer transformation cues. However, all of these still rely on bilinear sampling to transform the image.

3. Differentiating through interpolation

We now briefly review bilinear interpolation [17]; see Fig. 2. The main reason that a form of interpolation – typically bilinear interpolation – is used to implement differentiable image transformations is that transformations require indexing operations, which are not differentiable by themselves. More specifically, denoting the image coordinates as $\mathbf{x} \in \mathbb{R}^2$, the image intensity at this coordinate as $\mathbf{I}(\mathbf{x}) \in \mathbb{R}^C$, where C is the number of channels in the image, and the coordinate transformation with parameters $\boldsymbol{\theta}$ as $T_{\boldsymbol{\theta}}(\mathbf{x})$, then, the transformed image $\tilde{\mathbf{I}}$ evaluated at $\tilde{\mathbf{x}}$ is

$$\tilde{\mathbf{I}}(\tilde{\mathbf{x}}) = \sum_{\mathbf{x}} \mathbf{I}(T_{\boldsymbol{\theta}}(\mathbf{x}))\ K(\tilde{\mathbf{x}}, T_{\boldsymbol{\theta}}(\mathbf{x})), \tag{1}$$

where $K(\cdot,\cdot)$ is the kernel which defines the influence of each pixel. Note here that the image indexing operation $\mathbf{I}(T_{\boldsymbol{\theta}}(\mathbf{x}))$ is non-differentiable, as it is a selection operation, and the way gradients propagate through the network depends on the kernel. In theory, this kernel could leverage the entire image, thus making the gradient for all pixel values affect the optimization. However, this would require back-propagating through every pixel in the original image for every pixel in the transformed image, which is prohibitively expensive. In the case of bilinear interpolation, the kernel is set so that $K(\mathbf{x}, \mathbf{y}) = 0$ when $\mathbf{x}$ and $\mathbf{y}$ are not direct neighbors. Therefore, the gradient only flows through what we will refer to as *sub-pixel gradients*, *i.e*., the intensity difference between neighboring pixels in the *original* image.

This can be quite harmful under significant downsampling. The sub-pixel gradients will not correspond to the large-scale changes that occur when the transformation parameter changes, as these cannot be captured by the immediate neighbourhood of a point. In other words, the intensity values with non-zero gradients from kernel K need to be chosen in a way that is invariant to these deformations, and carefully so that it reflects how the image would actually change under deformations. We will now introduce a novel strategy to overcome this problem.

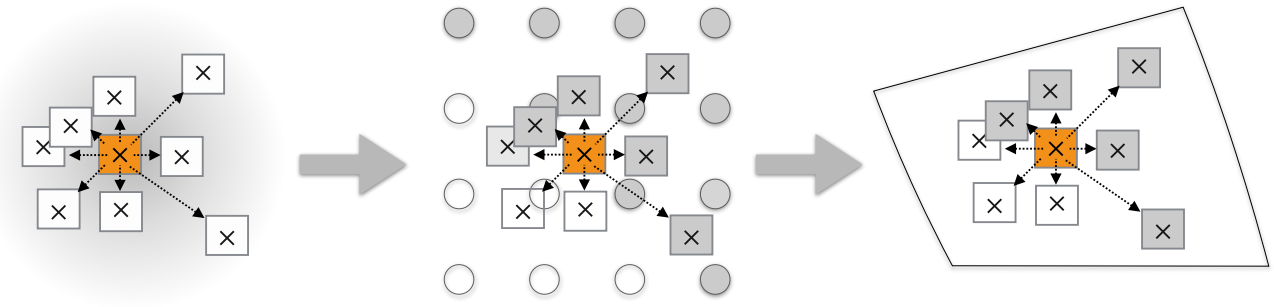
4. Linearized multi-sampling

Fig. 3 illustrates our method, step by step. Given a pixel location, we apply Gaussian noise to generate K nearby auxiliary sample locations. We then perform bilinear sampling at these locations. After sampling, we use the intensities of these points and their coordinates to perform a linear approximation at the sample location. Finally, these linear approximations are used as the differentiable representation of each pixel in the transformed image. This provides a larger context to the local transformation, and increases robustness under downsampling.

Formally, given the parameterization of the transformation $\boldsymbol{\theta}$, a desired sample point as $\mathbf{x}_i$, where i is the index for this sample, we write the linear approximation $\hat{\mathbf{I}}(\mathbf{x})$ as

$$\hat{\mathbf{I}}(\mathbf{x}) = \mathbf{I}(T_{\boldsymbol{\theta}}(\mathbf{x}_i)) + \mathbf{A}_i (T_{\boldsymbol{\theta}}(\mathbf{x}) - T_{\boldsymbol{\theta}}(\mathbf{x}_i)), \tag{2}$$

where $\mathbf{A}_i$ is a matrix that defines the linearization that we seek to find. For the sake of explanation, let us assume for the moment that we have $\mathbf{A}_i$. Then, notice here that we



Random samples generation | Bilinear sampling | Linearization

Figure 3: **Linearized multi-sampling –** For each pixel that we query, we generate a set of random auxiliary samples, whose intensities we extract through bilinear sampling. We then process these intensities to create a linear approximation, which we use as the differentiable representation for the intensity of the queried pixel.

are linearizing at the transformed coordinate $T_{\boldsymbol{\theta}}(\mathbf{x}_i)$, thus treating everything except for $T_{\boldsymbol{\theta}}(\mathbf{x})$ as a constant. Therefore, $\mathbf{A}_i$ in Eq. (2) corresponds to the gradient of $\hat{\mathbf{I}}(\mathbf{x})$ with respect to $\mathbf{x}$.

To obtain $\mathbf{A}_i$ we first sample multiple points near the desired sample points $\mathbf{x}_i$ and find a least-square fit for the sample results. Specifically, we take K samples

$$\mathbf{x}_i^k \sim \mathcal{N}(\mathbf{x}_i, \boldsymbol{\sigma}), \quad \forall k \in \{1, 2, ..., K\}, \tag{3}$$

where $\mathcal{N}(\boldsymbol{\mu}, \boldsymbol{\sigma})$ denotes a Gaussian distribution centered at $\boldsymbol{\mu}$ with standard deviation $\boldsymbol{\sigma}$, and $\mathbf{x}_i^0 = \mathbf{x}_i$. In our experiments we set $\boldsymbol{\sigma}$ to match the pixel width and height of the sample output. Note that by using Gaussian noise, we are effectively assuming a Gaussian point-spread function for each pixel when sampling.

We then obtain $\mathbf{A}_i$ by least-squares fitting. If we simplify the notation for $\tilde{\mathbf{I}}\left(T_{\boldsymbol{\theta}}\left(\mathbf{x}_i^k\right)\right)$ as $\tilde{\mathbf{I}}_i^k$, and for $T_{\boldsymbol{\theta}}\left(\mathbf{x}_i^k\right)$ as $\tilde{\mathbf{x}}_i^k$, where $\tilde{\mathbf{x}}_i^k = \left[\tilde{u}_i^k, \tilde{v}_i^k\right]$, we form two data matrices $\mathbf{Y}_i$ and $\mathbf{X}_i$, where

$$\mathbf{Y}_i = \mathbf{X}_i \mathbf{A}_i, \tag{4}$$

$$\mathbf{Y}_i = \left[\tilde{\mathbf{I}}_i^1 - \tilde{\mathbf{I}}_i^0 \quad \tilde{\mathbf{I}}_i^2 - \tilde{\mathbf{I}}_i^0 \quad \cdots \quad \tilde{\mathbf{I}}_i^{K-1} - \tilde{\mathbf{I}}_i^0\right]^\top, \tag{5}$$

$$\mathbf{X}_i = \begin{bmatrix} \tilde{u}_i^1 - \tilde{u}_i^0 & \tilde{u}_i^2 - \tilde{u}_i^0 & \cdots & \tilde{u}_i^{K-1} - \tilde{u}_i^0 \\ \tilde{v}_i^1 - \tilde{v}_i^0 & \tilde{v}_i^2 - \tilde{v}_i^0 & \cdots & \tilde{v}_i^{K-1} - \tilde{v}_i^0 \\ 1 & 1 & & 1 \end{bmatrix}^\top, \tag{6}$$

and then solve for A in a least square sense with Tikhonov regularization for numerical stability

$$\mathbf{A}_i = \left(\mathbf{X}_i^\top \mathbf{X}_i + \epsilon \mathbf{E}\right)^{-1} \mathbf{X}_i^\top \mathbf{Y}_i, \tag{7}$$

where $\mathbf{E}$ is the 3×3 identity matrix, and ϵ a small scalar.

Multi-scale sampling An alternative approach would be to use multi-scale alignment with auxiliary samples distributed over pre-defined grids at varying levels of coarseness. This can scale up as much as desired – potentially up to using the entire image as a neighborhood for each pixel – but the increase in computational cost is linear with respect to the number of auxiliary samples. Random selection allows us to capture both local and contextual structure in an efficient manner.

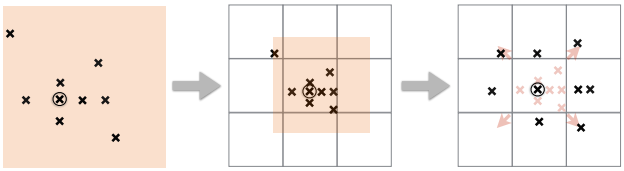


Figure 4: **Sample collapse prevention –** During an upsampling operation, the auxiliary samples (left) could fall onto a single pixel of the sampled image once the transformation is applied (middle). To prevent sample collapse, we apply additional noise to the *transformed* auxiliary sample locations (right).

5. Sample collapse prevention

While Eq. (7) is straightforward to compute, we need to take special care that the random samples do not collapse into a single pixel. This can happen when the transformation is zooming into a specific region; see Fig. 4 (middle). If this happens, the data matrix $\mathbf{X}_i$ generated from coordinate differences of transformed auxiliary samples will be composed of very small numbers, and the data matrix $\mathbf{Y}_i$, generated from difference in intensities, may also become zero. This leads to exploding gradients. To avoid them, we perturb the auxiliary samples *after* the transformation; see Fig. 4 (right). Denoting the modified coordinates for the k-th auxiliary sample for pixel i with $\tilde{u}_i^k$ and $\tilde{v}_i^k$, for $k \in \{1, 2, ..., K\}$, we then apply

$$\tilde{u}_i^k \leftarrow \tilde{u}_i^k + \mathcal{N}(0, \delta_u), \tag{8}$$

$$\tilde{v}_i^k \leftarrow \tilde{v}_i^k + \mathcal{N}(0, \delta_v), \tag{9}$$



Figure 5: **Dataset image examples –** (top-left) MNIST. (top-right) GTSRB. (bottom) Pascal VOC 2012.

where δ_u and δ_v correspond to the single pixel width and height in the image that we sample from – the magnitude of the transform in either dimension.

6. Results

To demonstrate the effectiveness of our method, we first present quantitative results on the performance of STN and ICSTN with different sampling methods. We show that the enhanced gradients from linearization-based sampling lead to significant improvements in the performance of deep networks, most prominently when downsampling is involved. We then visually inspect the gradients produced by bilinear sampling and our linearized multi-sampling approach, to demonstrate that the gradients produced by our method are more robust and lead to better convergence. We further show that this can be confirmed quantitatively by a simple image alignment task, performed with different sampling methods. Finally, we study the effect of the number of auxiliary samples and the impact of the magnitude of the sampling noise.

Datasets. Our experiments feature three datasets: MNIST [22], GTSRB [33], and Pascal VOC 2012 [13]; see Fig. 5. With MNIST, we show that our approach outperforms bilinear interpolation in one of the classical classification datasets. With GTSRB, we demonstrate that our method also leads to better performance in the more challenging case of classifying traffic sign images. Finally, we use Pascal VOC 2012 to showcase that the advantages of our method are even more prominent on natural images with richer textures.

Baselines. In addition to standard bilinear sampling, we also evaluate a multi-scale baseline where the image is sampled at multiple scales and then aggregated. This is similar to how multi-scale sampling with mipmaps is performed. To create a multi-scale representation, we create three scale levels, using Gaussian kernels with standard deviations $\{1, 5, 10\}$. We apply these sampling methods to STN [17] and ICSTN [23] for classification.

6.1. Implementation details

We implement our method with PyTorch [29], and use its default bilinear sampling to fetch the intensity corresponding to each of our random samples. Note that this sampling process is *not* differentiated through, and we use these intensities only to compute the linearization. To ensure this, our implementation explicitly stops the gradient from back-propagating for all variables except for $T_{\boldsymbol{\theta}}(\mathbf{x})$.

To prevent manifestation from out-of-bound samples, we simply mask the sample points that fall outside the original image. Specifically, for each pixel i, if $T_{\boldsymbol{\theta}}\left(\mathbf{x}_i^k\right)$ is out of bounds, we exclude it from Eq. (5) and Eq. (6). This can be easily achieved by multiplying the corresponding entries with zero. When all pixels are out of bounds, $\mathbf{A}_i$ becomes a zero matrix, thus providing a zero gradient.

Throughout our experiments, we use eight auxiliary samples per pixel ($K = 8$), a choice we will substantiate in Section 6.5.

6.2. Classification

To demonstrate that sampling plays a critical role in networks that contain image transformations, we train a network for image classification with STN/ICSTN prepended to it on the GTSRB dataset. We emulate a standard setup used to leverage attention mechanisms by using STN/ICSTN to produce a transformation of a smaller resolution than the input image, which is then given to the classifier – the task of STN/ICSTN is thus to focus on a single region that helps to classify traffic signs. We evaluate the accuracy of the classifier under different downsampling

Table 1: Test error of models trained with various sampling methods, using STN and ICSTN. Best results are marked in bold. Our method gives best performance even when there is no downsampling, and the gap widens at higher downsampling rates.

Downsampling rate # classif. network param.	1x 966k	2x 246k	4x 61k	8x 19k
Baseline w/o STN	12.37	12.88	20.85	45.88
STN + Bilinear	6.29	6.50	7.95	15.31
STN + Multi-scale	6.83	6.70	8.30	15.00
STN + Ours	**6.08**	**6.48**	**7.13**	**10.89**
ICSTN + Bilinear	5.68	5.00	6.52	9.80
ICSTN + Multi-scale	5.40	5.95	6.06	10.19
ICSTN + Ours	**4.85**	**4.68**	**4.86**	**6.10**

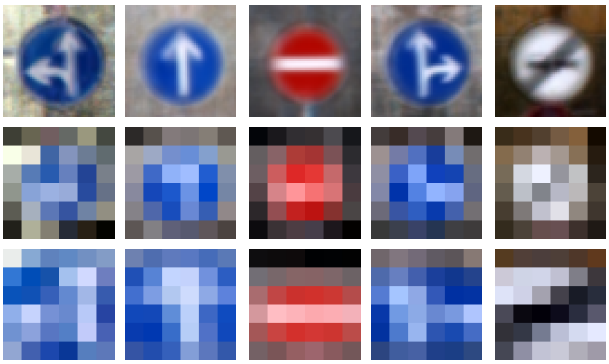


Figure 6: **Example outputs of trained STN modules –** Outputs of STNs trained on the 8x downsampled GTSRB dataset (top) with bilinear sampling (middle) and our approach (bottom). The STN trained with our linearized sampling scheme learns to zoom-in for better classification accuracy.

rates. We detail this experiment and the results below.

Network architecture and training setup. To train the network we randomly split the training set of GTSRB into two sets, 35309 images for training and 3900 for validation. For testing we use the provided test set that holds 12630 images. We crop and resize all images to 50×50.

For the STN/ICSTN module, denoting convolution layers with c channels as $C(c)$, ReLU activations as R, and max-pooling layers as P, our network is: $C(4)RC(8)RPC(16)RPC(32)RPC(1024)$. All convolutional layers use 7×7 kernels. We apply max-pooling over each channel of the last feature map to produce one feature vector of size 1024. We then apply a fully connected layer with 48 neurons and ReLU activations, followed by another fully connected layer that maps to transformation parameters – translation, scale, and rotation in our experiments.

For the classification network, we use a simple network with a single hidden layer with 128 neurons and ReLU activations. We choose a simple architecture on purpose in order to prevent the network relying on the increased capacity of a large classification network and learn spatial invariance and effectively ignoring the STN.

We use ADAM [20] as the optimizer, and choose 10^{-5} and 10^{-3} as the learning rates for the STN/ICSTN modules and the classifier respectively. We train the models from scratch with a batch size of 64, and set the maximum number of iterations to 300k. We use early stopping if the model shows no improvement on the validation split within the last 80k iterations.

Results. In Table 1 we show the test accuracy of our approach compared to bilinear sampling and multi-scale sampling, with both STN and ICSTN. Unsurprisingly, the performance of both degrades as downsampling becomes more severe, but significantly less so with our method. Notably, the network trained with our sampling method performs the best for *all* downsampling rates – even without any downsampling. Moreover, with ICSTN and our method, there is no noticeable performance degradation even with 4x downsampling, allowing the classification network to be 11 times smaller compared to when no downsampling is used.

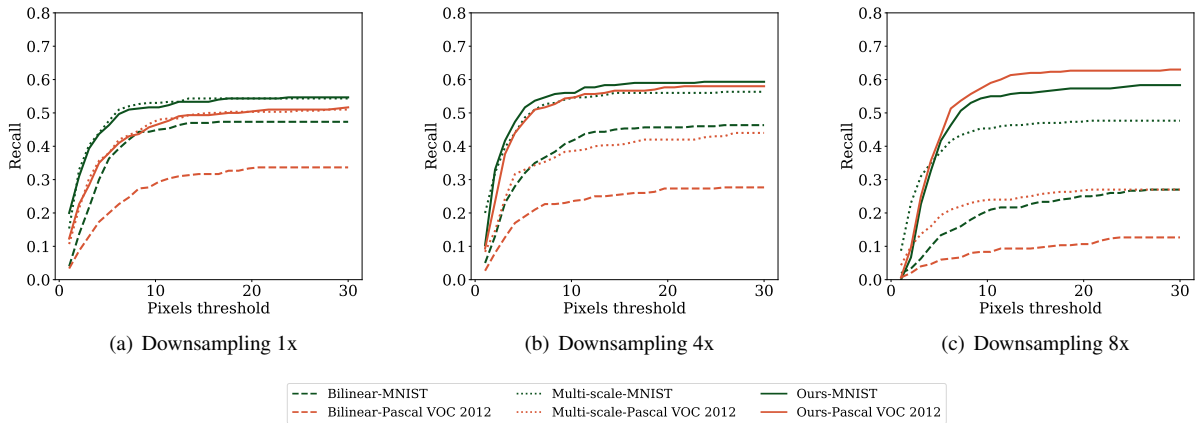
Finally, we show the average transformed image for a subset of the classes in the test set in Fig. 6. Note how the outputs of our network are zoomed-in with respect to the original input image, and more so than the results with bilinear sampling. This shows that with our linearized sampling strategy the network learns to focus on important regions more effectively.

6.3. Gradient analysis

To understand where such a drastic difference comes from, we show how the gradients produced by our approach differ from those of bilinear sampling. We compare how the gradients flow when we artificially crop the central region of an image, move it to a different location, and ask the STN to move it back to the original position. We use natural images from the Pascal VOC dataset for this purpose. Specifically, we crop the central two-thirds of the image, downsample them at different rates with bilinear interpolation, and use this image as our guidance for the STN with an ℓ_2 loss.

In Fig. 8 we visualize the negative gradient flows, *i.e.* the direction of steepest descent, extracted on a coarse grid on top of the image for which the gradients were computed.

Since the target area is the central region, the gradients should all point towards the center. As shown, our method provides a wider basin of convergence, having the gradients consistently point towards the center, *i.e.*, the ground truth location, from points further away than with bilinear sampling. Note that while this has a drastic effect for the case



(a) Downsampling 1x (b) Downsampling 4x (c) Downsampling 8x

Figure 7: **Image alignment experiments –** We threshold based on the average re-projection error of the four corners of the sampled region. Our method (solid line) performs well even under high downsampling rates, whereas the performance with bilinear sampling (dashed line) and multiscale sampling (dotted line) drops drastically. Note also that the gap is even larger for natural images (orange).

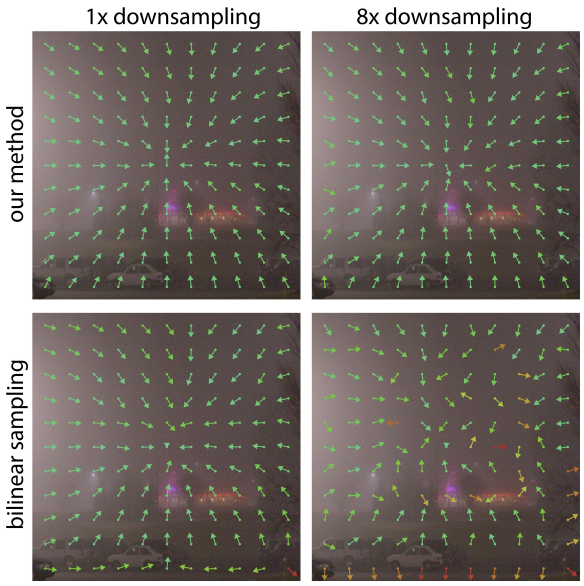


Figure 8: Gradients produced by our method vs bilinear sampling, evaluated across two downsampling factors. The (negated) image alignment gradients are visualized with arrows, colored from green to red according to whether they match the ground truth (all arrows should point towards the center). Our method shows a wider basin of convergence than bilinear sampling. The difference becomes more prominent as the downsampling rate increases. Even without downsampling, we provide better gradients.

of downsampling by 8x, it holds true even when there is no downsampling (Fig. 8, left). This is particularly distinctive around the bottom of the image, which has richer structures than the rest, which is blurry and thus rather smooth. This causes bilinear sampling to provide poor gradients, whereas our method is not susceptible to this.

6.4. Optimizing for image alignment

Next, we demonstrate that this improvement in the gradients produced by our approach leads to better outcomes when *aligning* images, as illustrated earlier in Fig. 1. In order to isolate the effect of the sampler, we exclude the classification network and directly optimize the parameters of a STN for one image at a time, with a single synthetic perturbation. We then evaluate the quality of the alignment after convergence. We repeat this experiment 80 times, on randomly selected images from the different datasets, and with random transformations.

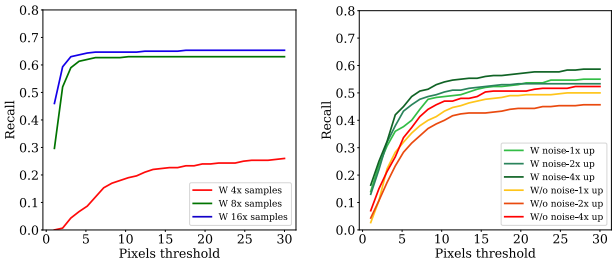
For the perturbations, we apply random in-plane rotations, scale changes (represented in log-space, *i.e.* scale of 0.5 is represented as -1) in the horizontal and vertical directions (independently), and translations. We sample Gaussian noise with standard deviation of 1 and apply it as follows. With the image coordinates normalized to $[-1, 1]$, we use a standard deviation of $\pi/4$ for rotations, $\sqrt{2}$ for scale changes in horizontal and vertical directions separately, and 0.2 for translations.

We summarize our image alignment experiments in Fig. 7. As shown, our results are significantly better than those of bilinear sampling, even when there is no downsampling. We also outperform the multi-scale if there is any downsampling at all. More importantly, the gap between methods is specially wide on natural images, where the image characteristics are much more complex than for the other two datasets. Finally, the effects of downsampling become quite severe at 8x, effectively breaking the bilinear sampler and the multi-scale approach in all datasets, and for PASCAL VOC in particular.



(a) Recall vs threshold (b) $\sigma = 1$px (c) $\sigma = 3$px (d) $\sigma = 6$px

Figure 9: **Ablation test for σ –** Effect of the magnitude of the noise used to generate the auxiliary samples. (**a**) Quantitative results in terms of recall vs threshold. (**b-d**) The spatial context increases along with the noise (left to right), as the auxiliary samples spread out, as indicated by the blurring. In (**a**), more noise results in more spatial context thus a larger basin of convergence, but at the cost of final accuracy. Also, as shown in (**b-d**), the image becomes more blurry as compromise.



(a) (b)

Figure 10: **Ablation test on the number of samples –** Effect of (**a**) number of samples on image alignment under 4x downsampling, and (**b**) sample collapse prevention under 1x, 2x, and 4x upsampling. Both are in terms of recall vs threshold. We again use the average reprojection error of four corners of the sampled region. In (**a**), increasing the number of samples provides better results in terms of alignment. In (**b**), we demonstrate that sample collapse prevention is essential when upsampling.

6.5. Ablation tests

Auxiliary sample noise. We also examine the effect of the magnitude of the noise we use to place the auxiliary samples in Eq. (3). Fig. 9 (b-c) shows the sampling result under various σ. Since the Gaussian noise emulates a point spread function, with a larger σ we obtain a blurrier image via Eq. (1). While the outcome is blurry, this effectively allows our method to consider a wider support region in the computation of the gradients, which will therefore be smoother. As shown in Fig. 9 (a), the wider spatial extent covered by the random samples translates into better image alignment results in the Pascal VOC dataset.

Number of auxiliary samples. In Fig. 10 (a) we evaluate the effect of number of random samples taken for each pixel with the Pascal VOC dataset under 4x downsampling. As expected, increasing the number of auxiliary samples leads to better alignment results. When only four auxiliary samples are used, the linearization is quite ill-conditioned and thus accuracy of the method drops.

Sample collapse avoidance. In Fig. 10 (b) we demonstrate the importance of the sample collapse prevention scheme described in Section 5. When our technique for sample collapse prevention is removed, the performance in image alignment drops due to the numerical instability caused by all auxiliary samples falling in the same neighbourhood. By contrast, our approach prevents this problem.

7. Conclusions and future work

We have proposed a linearization method based on multi-sampling to improve the poor gradients provided by bilinear sampling – a de-facto standard for differentiable image manipulation, typically within Spatial Transformers – for example, to implement hard attention. We have demonstrated empirically that our method can provide improved gradients, leading to enhanced performance on downstream tasks. Our approach simply swaps the sampler used by networks that rely on Spatial Transformers, and is thus compatible with any improvements that build on top of them.

Note that it is possible to replace the sampler with bilinear interpolation at inference time to preserve efficiency. As of now, this would result in a minor change in the sampling outcome and require fine tuning of the classifier. As immediate future work, we are currently investigating a bias-free formulation for Eq. (6), which would allow in-place replacement without further fine tuning.

Acknowledgements

This work was partially supported by the Natural Sciences and Engineering Research Council of Canada Discovery Grant "Deep Visual Geometry Machines" (RGPIN-2018-03788, DGECR-2018-00426), Google, and by systems supplied by Compute Canada.

References

[1] Hani Altwaijry, Eduard Trulls, James Hays, Pascal Fua, and Serge Belongie. Learning to Match Aerial Images with Deep Attentive Architecture. In *CVPR*, 2016. 1

[2] Simon Baker and Iain Matthews. Lucas-Kanade 20 Years On: A Unifying Framework. *IJCV*, pages 221–255, March 2004. 2

[3] John Leonard Barron, David J Fleet, and Steven Simon Beauchemin. Performance of Optical Flow Techniques. *IJCV*, 12:43–77, 1994. 2

[4] Chandrasekhar Bhagavatula, Chenchen Zhu, Khoa Luu, and Marios Savvides. Faster Than Real-time Facial Alignment: A 3D Spatial Transformer Network Approach in Unconstrained Poses. In *ICCV*, volume 2, page 7, 2017. 2

[5] Antoni Buades, Bartomeu Coll, and Jean-Michel Morel. A Non-Local Algorithm for Image Denoising. In *CVPR*, 2005. 2

[6] Che-Han Chang, Chun-Nan Chou, and Edward Y. Chang. CLKN: Cascaded Lucas-Kanade Networks for Image Alignment. In *CVPR*, 2017. 3

[7] Liang-Chieh Chen, George Papandreou, Iasonas Kokkinos, Kevin Murphy, and Alan L. Yuille. DeepLab: Semantic Image Segmentation with Deep Convolutional Nets, Atrous Convolution, and Fully Connected CRFs. *PAMI*, 2018. 3

[8] Xianjie Chen and Alan L. Yuille. Articulated Pose Estimation by a Graphical Model with Image Dependent Pairwise Relations. In *NIPS*, 2014. 2

[9] Yi Chen, Nasser M. Nasrabadi, and Trac D. Tran. Hyperspectral Image Classification Using Dictionary-Based Sparse Representation. *TGRS*, 49(10):3973–3985, 2011. 2

[10] Jifeng Dai, Haozhi Qi, Yuwen Xiong, Yi Li, Guodong Zhang, Han Hu, and Yichen Wei. Deformable Convolutional Networks. In *ICCV*, 2017. 1

[11] Patrick Ebel, Anastasiia Mishchuk, Kwang Moo Yi, Pascal Fua, and Eduard Trulls. Beyond cartesian representations for local descriptors. In *ICCV*, 2019. 2

[12] Carlos Esteves, Christine Allen-Blanchette, Xiaowei Zhou, and Kostas Daniilidis. Polar transformer networks. In *ICLR*, 2018. 2

[13] Mark Everingham, Luc Van Gool, Christopher K. I. Williams, John Winn, and Andrew Zisserman. The PASCAL Visual Object Classes Challenge 2012 (VOC2012) Results. http://www.pascal-network.org/challenges/VOC/voc2012/workshop/index.html. 5

[14] Clément Godard, Oisin Mac Aodha, and Gabriel J. Brostow. Unsupervised Monocular Depth Estimation with Left-Right Consistency. In *CVPR*, page 7, 2017. 3

[15] Kaiming He, Georgia Gkioxari, Piotr Dollár, and Ross Girshick. Mask R-CNN. In *ICCV*, 2017. 1, 3

[16] Kaiming He, Jian Sun, and Xiaoou Tang. Guided Image Filtering. *PAMI*, (6):1397–1409, 2013. 2

[17] Max Jaderberg, Karen Simonyan, Andrew Zisserman, and Koray Kavukcuoglu. Spatial Transformer Networks. In *NIPS*, pages 2017–2025, 2015. 1, 2, 3, 5

[18] Zhiwei Jia, Haoshen Hong, Siyang Wang, Kwonjoon Lee, and Zhuowen Tu. Controllable Top-down Feature Transformer. *arXiv Preprint*, 2018. 2, 3

[19] Justin Johnson, Andrej Karpathy, and Li Fei-fei. Densecap: Fully Convolutional Localization Networks for Dense Captioning. In *CVPR*, 2016. 1

[20] Diederik P. Kingma and Jimmy Ba. Adam: A Method for Stochastic Optimization. *arXiv Preprint*, 2014. 6

[21] Jason Kuen, Zhenhua Wang, and Gang Wang. Recurrent Attentional Networks for Saliency Detection. In *CVPR*, 2016. 1

[22] Yann LeCun, Léon Bottou, Yoshua Bengio, and Patrick Haffner. Gradient-Based Learning Applied to Document Recognition. In *Proceedings of the IEEE*, pages 2278–2324, 1998. 5

[23] Chen-Hsuan Lin and Simon Lucey. Inverse Compositional Spatial Transformer Networks. *CVPR*, 2017. 1, 2, 3, 5, 11

[24] Shu Liu, Lu Qi, Haifang Qin, Jianping Shi, and Jiaya Jia. Path Aggregation Network for Instance Segmentation. In *CVPR*, pages 8759–8768, 2018. 1

[25] Jonathan Long, Evan Shelhamer, and Trevor Darrell. Fully Convolutional Networks for Semantic Segmentation. In *CVPR*, 2015. 3

[26] Bruce D. Lucas and Takeo Kanade. An Iterative Image Registration Technique with an Application to Stereo Vision. In *IJCAI*, pages 674–679, 1981. 2

[27] Dmytro Mishkin, Filip Radenovic, and Jiri Matas. Repeatability Is Not Enough: Learning Affine Regions via Discriminability. In *ECCV*, 2018. 1, 2

[28] Yuki Ono, Eduard Trulls, Pascal Fua, and Kwang Moo Yi. Lf-Net: Learning Local Features from Images. In *NIPS*, 2018. 1, 2

[29] Adam Paszke, Sam Gross, Soumith Chintala, Gregory Chanan, Edward Yang, Zachary DeVito, Zeming Lin, Alban Desmaison, Luca Antiga, and Adam Lerer. Automatic Differentiation in Pytorch. In *NIPS*, 2017. 5

[30] Charles R. Qi, Hao Su, Kaichun Mo, and Leonidas J. Guibas. Pointnet: Deep Learning on Point Sets for 3D Classification and Segmentation. In *CVPR*, 2017. 2

[31] Olaf Ronneberger, Philipp Fischer, and Thomas Brox. U-Net: Convolutional Networks for Biomedical Image Segmentation. In *MICCAI*, 2015. 3

[32] Chang Shu, Xi Chen, Qiwei Xie, and Hua Han. Hierarchical Spatial Transformer Network. *arXiv Preprint*, 2018. 2, 3

[33] Johannes Stallkamp, Marc Schlipsing, Jan Salmen, and Christian Igel. The German Traffic Sign Recognition Benchmark: A multi-class classification competition. *IJCNN*, 2011. 5

[34] David Joseph Tan, Thomas Cashman, Jonathan Taylor, Andrew Fitzgibbon, Daniel Tarlow, Sameh Khamis, Shahram Izadi, and Jamie Shotton. Fits Like a Glove: Rapid and Reliable Hand Shape Personalization. In *CVPR*, 2016. 2

[35] Fangfang Wang, Liming Zhao, Xi Li, Xinchao Wang, and Dacheng Tao. Geometry-Aware Scene Text Detection with Instance Transformation Network. In *CVPR*, 2018. 2

[36] Wanglong Wu, Meina Kan, Xin Liu, Yi Yang, Shiguang Shan, and Xilin Chen. Recursive Spatial Transformer

(ReST) for Alignment-Free Face Recognition. In *CVPR*, pages 3772–3780, 2017. 2

[37] Kwang Moo Yi, Eduard Trulls, Vincent Lepetit, and Pascal Fua. LIFT: Learned Invariant Feature Transform. In *ECCV*, 2016. 1, 2

[38] Kwang Moo Yi, Yannick Verdie, Pascal Fua, and Vincent Lepetit. Learning to Assign Orientations to Feature Points. In *CVPR*, 2016. 1

[39] Haoyang Zhang and Xuming He. Deep Free-Form Deformation Network for Object-Mask Registration. In *CVPR*, pages 4251–4259, 2017. 2

[40] Hongyan Zhang, Jiayi Li, Yuancheng Huang, and Liangpei Zhang. A Nonlocal Weighted Joint Sparse Representation Classification Method for Hyperspectral Imagery. *J-STARS*, 7(6):2056–2065, 2014. 2

A. Supplementary appendix

A.1. Computation time

The amount of overhead depends on the number of auxiliary samples, and the size of the input images. The increase is mainly in the backward pass. With default parameters, our method runs on average at a speed of 67% compared to bilinear sampling for the forward pass, and 40% for the backward pass.

A.2. Results on MNIST

As MNIST dataset is textureless, both sampling methods perform similarly – we used the implementation of [23] and achieved 1.4% error rate for both bilinear sampling and ours. While the two perform similar, as shown on the average aligned image below, ours zooms in more on digits.

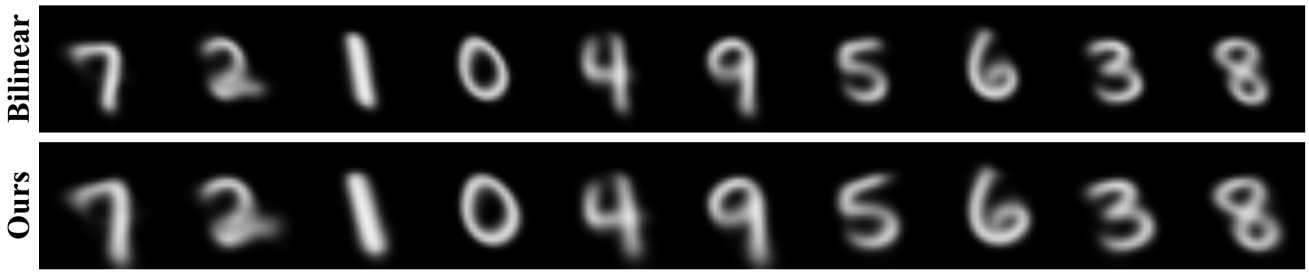


Figure 11: Average aligned image from the STN using (top) bilinear sampling and (bottom) our method.